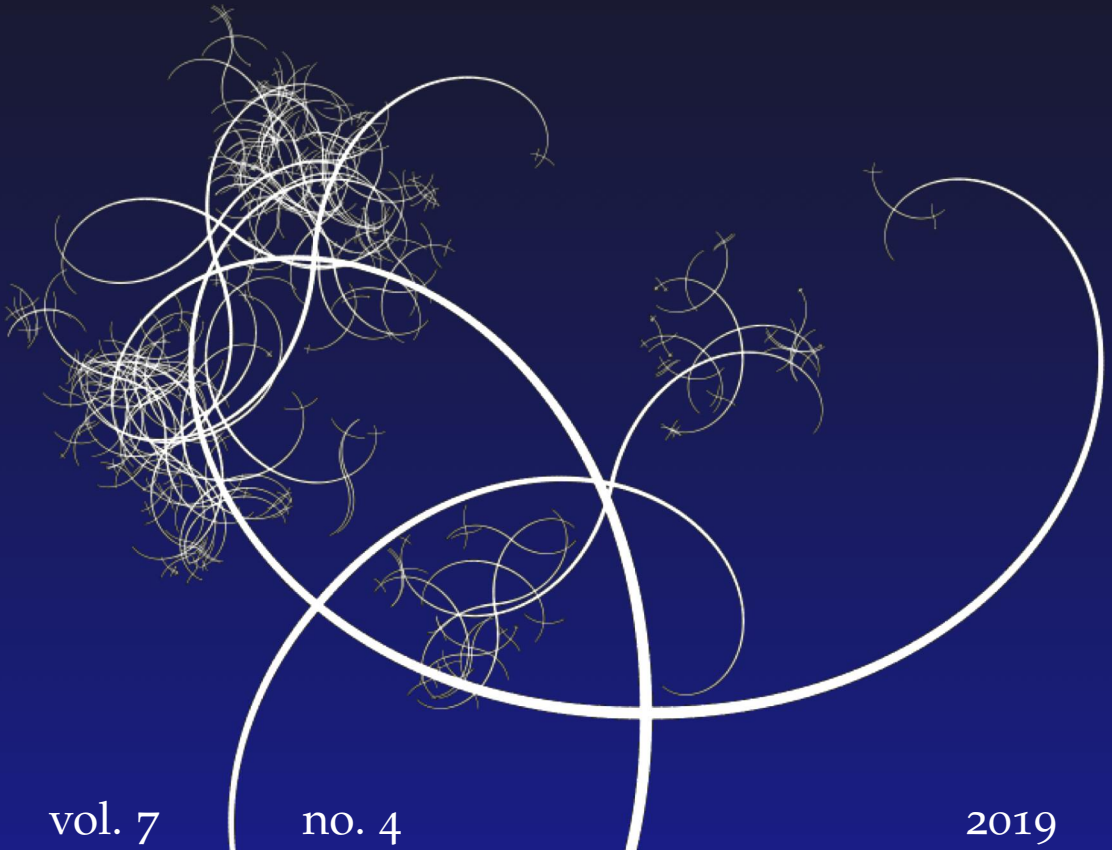


NISSUNA UMANA INVESTIGAZIONE SI PUO DIMANDARE VERA SCIENZA
S'ESSA NON PASSA PER LE MATEMATICHE DIMOSTRAZIONI
LEONARDO DA VINCI



vol. 7

no. 4

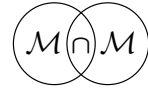
2019

MATHEMATICS AND MECHANICS
of
Complex Systems

EMILIO TURCO AND EMILIO BARCHIESI

EQUILIBRIUM PATHS OF HENCKY PANTOGRAPHIC BEAMS IN A
THREE-POINT BENDING PROBLEM





EQUILIBRIUM PATHS OF HENCKY PANTOGRAPHIC BEAMS IN A THREE-POINT BENDING PROBLEM

EMILIO TURCO AND EMILIO BARCHIESI

We investigate the mechanical behavior of so-called pantographic beams undergoing large deformations. To this aim, an exact-kinematics Hencky pantographic beam model has been employed in a three-point bending test. Given the occurrence of local snap-through instabilities and limit points, said Hencky model has been solved by means of a step-by-step strategy based on Riks's arc-length method. Such a method has been particularly adapted for the case of problems with prescribed displacements, as opposed to those with prescribed forces. Numerical simulations performed by varying the stiffness parameters are discussed, aimed at getting an insight into the different behaviors which can be exhibited by pantographic beams. Numerical simulations performed by varying the quantity of unit cells for fixed total length allow instead to understand whether the observed features are inherent to the pantographic beam structure or size-dependent. Therefore, beyond being interesting for possible future engineering exploitation, we believe this phenomenological evidence to be useful in guiding the formulation of conjectures regarding observed microscale local snap-through instability phenomena in the framework of a previously proposed macroscale continuum model for pantographic beams obtained by asymptotic homogenization.

1. Introduction

In the recent literature, it has been widely argued, both experimentally and theoretically, that pantographic structures are very effective in reaching large total deformations while still operating in the elastic regime (see the review papers [dell'Isola et al. 2019a; 2019b] for a detailed introduction on pantographic structure properties and [dell'Isola et al. 2016] for an efficient and predictive model of such structures). Nevertheless, their properties at microscale induce further exotic properties at macroscale which can be exploited in several engineering applications. For instance, due to their characteristic accordion-like zero-energy mode, they may

Communicated by Pierre Seppecher.

Turco is the corresponding author.

MSC2010: 74B20.

Keywords: pantographic beams, Lagrangian models, nonlinear analysis.

be used to build reconfigurable structures such as those reported in [Filipov et al. 2015]. A quantitative account of deformation mechanisms in unit elements of pantographic structures — including pantographic beams studied herein — has been given in [Turco et al. 2017a; 2019b], thus providing a way of assessing experimentally stiffnesses employed in Hencky modeling of such structures.

A kind of slender pantographic structure, the so-called pantographic beam, has been introduced in the literature as a microstructure leading by asymptotic homogenization to a complete second-gradient beam at macroscopic scale, which means a continuum beam model with elastic deformation energy depending on the projection of the second placement material gradient onto both the normal vector to the deformed centerline — i.e., the material curvature — and the tangent one — i.e., the stretch gradient [Alibert et al. 2003; Barchiesi et al. 2018; 2019]. It has been demonstrated that, beyond the capacity of sustaining nonstandard boundary external actions like double-forces, unusual elastic nonlinear behaviors — like softening and apparent negative stiffness — can arise in the equilibrium path of such structures in, e.g., the three-point bending problem due to gradient behavior in extension.

In this work we focus on modeling by the Hencky approach [Turco et al. 2016c], with such pantographic beams subjected to a three-point bending test, and we aim to explore their nonlinear behaviors. As reported in the review paper [Bertoldi et al. 2017], there is a plethora of possible and fruitful applications which can take advantage of instability phenomena. In particular, one may conceive technical applications which exploit (i) the presence of buckling loads, e.g., to reach large reversible deformations triggered by loads fulfilling threshold criteria, (ii) multistability, i.e., the capability of snapping between two (or more) stable equilibrium configurations, or (iii) the possibility of introducing controlled defects to obtain multistability and, in general, to fine-tune the structural response so as to exhibit a desired behavior. If one considers that pantographic beams can be built at micrometer scale using the technology reported in [dell’Isola et al. 2019c], then all above points become actual and profitable possibilities.

Degenerate behaviors [Barchiesi et al. 2018; 2019] in the above-mentioned homogenized continuum model, i.e., local phase transition from flexible beam to cable, which can origin from local snap-through instabilities at microscale, for sufficiently large prescribed displacements, have been previously discussed. Approaching limit points of the equilibrium path — whose occurrence had been observed previously with discrete and continuum models — as well as when local snap-through instabilities occur, the analysis of the discrete model by means of numerical schemes based on the Newton–Raphson algorithm gets extremely ineffective. In such cases, e.g., Riks-like algorithms should be considered [Riks 1972]. In what follows we shortly introduce discrete model kinematics and deformation

energy. We subsequently recall the employed Riks-like numerical method and so-called three-point bending problem for a discrete Hencky pantographic beam. We carry out a parametric study in order to explore the possible achievable nonlinear behaviors. It turns out as a novel result that the strongly nonlinear behavior of discrete pantographic beams is very rich and characterized by the occurrence of multiple limit points, by negative stiffness regions of the equilibrium path, and by the occurrence of local snap-through instability phenomena. These phenomena provide a strong microscale-based support to the formulation of conjectures regarding local beam-to-cable transitions in corresponding homogenized continua, which is one of the main motivations stimulating the present study.

2. Lagrangian modeling

We consider a straight pantographic beam in-plane such as that represented in Figure 1 (top). It consists of two families of extensional-bending bars connected in the intersecting midpoints by torsion links. Owing to previous experience in the realization and modeling of such links and said extensional-bending bars, we adopt the description depicted in Figure 1 (bottom) based on spring assemblies; see [Turco et al. 2016a; 2016b; 2016e; Turco and Rizzi 2016] for a description of the predictive capability of such a model, [Turco et al. 2017b] for a first attempt to optimize fiber orientation, and [Turco et al. 2018] for an enhanced Hencky model

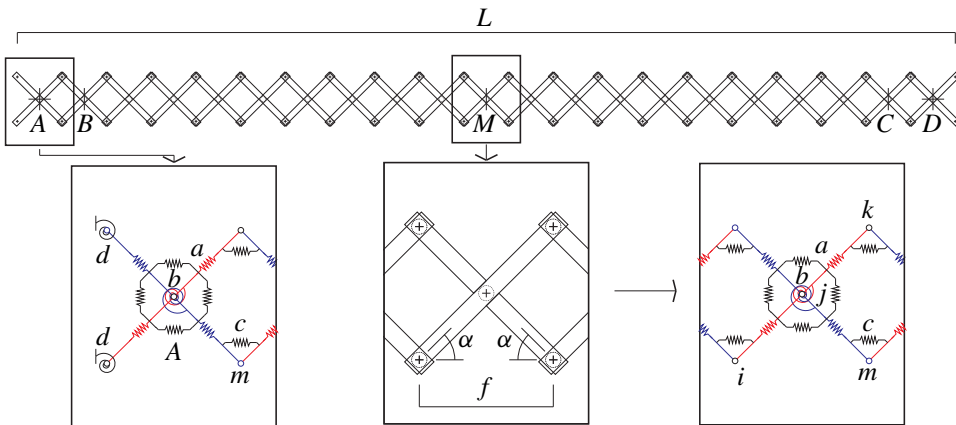


Figure 1. Geometry and Hencky model of considered pantographic beam (oblique bars form an angle $\alpha = \pi/4$ with the horizontal line). In the three-point bending problem displacements of points A and D , as well as vertical displacements of points B and C , are set to be zero, while vertical displacement of the midpoint M is fixed to a value different from zero.

in pantographic structures with perfect pivots, i.e., pivots which behave as perfect hinges.

The finite-strain constitutive behaviors of elastically deformable links in the pantographic beam are the following ones, as expressed by means of stored deformation energies:

$$\begin{aligned}
 E_a &= \frac{1}{2}a\Delta\ell^2, \\
 E_b &= b(1 + \cos\beta), \\
 E_c &= \frac{1}{2}c\left(\gamma - \frac{1}{2}\pi\right)^2, \\
 E_d &= d\left(1 - \cos\left(\delta - \frac{1}{4}\pi\right)\right),
 \end{aligned} \tag{1}$$

with E_a , E_b , E_c , and E_d being the strain energies stored, respectively, in the extensional springs, depicted in red and blue in Figure 1, flexural-rotational springs, depicted in red and blue in Figure 1, shearing-rotational springs, depicted in black in Figure 1, and flexural-rotational springs on the left and right ends of the pantographic beam, depicted in black in Figure 1. The stiffnesses of the above-mentioned springs are denoted by a , b , c , and d , respectively;¹ the associated strain measures $\Delta\ell$ (stretching), $\cos\beta$ (bending), γ (shearing), and δ (rotation) are all defined as functions of the current positions of nodes of the pantographic beam or, in other words, as functions of nodal displacements (nodes are depicted in Figure 1 as small circles located at the intersection points of the oblique bars) with respect to the reference configurations. Therefore, strain measures can be written as

$$\begin{aligned}
 \Delta\ell &= \|p_j - p_i\| - \|P_j - P_i\|, \\
 \cos\beta &= \frac{\|p_j - p_i\|^2 + \|p_k - p_j\|^2 - \|p_k - p_i\|^2}{2\|p_j - p_i\|\|p_k - p_j\|}, \\
 \gamma &= \arccos \frac{\|p_j - p_m\|^2 + \|p_k - p_j\|^2 - \|p_k - p_m\|^2}{2\|p_j - p_m\|\|p_k - p_j\|}, \\
 \cos\left(\delta - \frac{1}{4}\pi\right) &= \frac{\mathbf{v} \cdot \mathbf{e}_1 + \mathbf{v} \cdot \mathbf{e}_2}{\|P_j - P_i\|^2},
 \end{aligned} \tag{2}$$

where P_i and p_i are the reference and the current positions of node i (the same is true for nodes j , k , and m), respectively, $\mathbf{v} = (p_j - p_i) - (P_j - P_i)$, and \mathbf{e}_1 , \mathbf{e}_2 are the horizontal and vertical unit vectors (more details on this can be found in [Turco et al. 2016c]). Strain energies for each spring of the considered lattice completely define its mechanical behavior. We remark that the strain energy E_b differs from

¹Intentionally, although it would be possible, we do not assume as different the stiffnesses of the two families of oblique bars (red and blue rotational and extensional springs); at the same time we consider only one parameter c to describe the shearing stiffness (black rotational springs) and one parameter d to describe the flexural-rotational one on the left and right ends of the pantographic beam.

that in [Barchiesi et al. 2018; 2019], which reads as $E_b = (b/2)(\beta - \pi)^2$. It is easy to see that for β in a small neighborhood of π (i.e., the value assumed by β in the reference zero-energy configuration) the two choices for E_b are equivalent. Nevertheless, even for a relatively large neighborhoods — e.g., $\pi - 1 \leq \beta \leq \pi + 1$ (this neighborhood includes all values assumed by β in the present analysis — it can be seen a posteriori) — the two energies behave so similarly as to give the same results for the scopes of the present analysis. This also shall motivate that for meaningfully relating discrete and continuum derivations, later on, we will use the same scaling law (see (14)) used in the continuum derivation [Barchiesi et al. 2018; 2019]. Defining the structural reaction of the system as the gradient of the total potential energy² with respect to independent Lagrangian variables — e.g., nodal displacements — the stationarity condition for the potential energy with respect to independent Lagrangian variables, i.e., equating to zero the structural reaction, gives equilibrium equations. The Hessian matrix, which collects the second partial derivatives of the strain energy with respect to independent Lagrangian variables, is the so-called stiffness matrix of the system. The equilibrium equations and stiffness matrix of the considered system are the only tools which are necessary to code a step-by-step procedure such as that reported in the following section.

3. Recovering the equilibrium path

The nonlinear system of equilibrium equations derived by enforcing the stationarity condition for the potential energy with respect to nodal displacements reads as

$$s[\mathbf{u}, \lambda \bar{\mathbf{u}}] = \mathbf{0}, \quad (3)$$

with s being the structural reaction depending upon vectors \mathbf{u} and $\lambda \bar{\mathbf{u}}$. The vector \mathbf{u} collects nodal displacements relative to the nodes which are free to be displaced, while the vector $\bar{\mathbf{u}}$ collects those nodal constrained displacements scaled by the real parameter λ . We remark that this kind of problem, i.e., a problem with constrained displacements on a subset of nodal displacements, is not usual in technical literature with few exceptions [Turco 2018b; Turco et al. 2019a]. Therefore, we report below a brief description of the used method and the final formulae. We further explicitly remark that λ , still being the parameter which scales the nodal constrained displacements to give $\bar{\mathbf{u}}$, is also the value of the only nonzero constrained (vertical) displacement, i.e., that at the middle of the beam (node M).

The solution of the nonlinear system of equations (3) in the unknown nodal displacements can be achieved by using a step-by-step procedure based on Newton's method. If the pair $(\mathbf{u}_i, \lambda_i)$ — where index i is not referring to node numbering

²Potential and strain energy are the same in the considered case, since the work of external loads is zero.

as in (2) but to iterations of a recursive procedure — represents an equilibrium point, that is $s[\mathbf{u}_i, \lambda_i \bar{\mathbf{u}}] = \mathbf{0}$, then — notwithstanding that there may be multiple equilibrium points for fixed $\Delta\lambda$ — we can estimate a further close equilibrium point $(\mathbf{u}_i + \Delta\mathbf{u}, \lambda_i + \Delta\lambda)$ by linearizing (3):

$$s[\mathbf{u}_i, \lambda_i \bar{\mathbf{u}}] + \mathbf{K}_{uu} \Delta\mathbf{u} + \mathbf{K}_{u\bar{u}} \Delta\lambda \bar{\mathbf{u}} \approx \mathbf{0}, \quad (4)$$

where \mathbf{K}_{uu} and $\mathbf{K}_{u\bar{u}}$ are submatrices of the stiffness matrix \mathbf{K} , computed in $(\mathbf{u}_i, \lambda_i)$, whose rows correspond to the variables collected in the vector \mathbf{u} and whose columns correspond to the variables collected in the vectors \mathbf{u} and $\bar{\mathbf{u}}$, respectively. The same notation will be used to indicate submatrices of the stiffness matrix in the sequel.

We can then estimate for a chosen $\Delta\lambda$ — which should be small enough so that the point fulfills up to a given residual tolerance the equilibrium equations — unknown displacements as the sum of \mathbf{u}_i and the increment of displacements $\Delta\mathbf{u}$ found as

$$\Delta\mathbf{u} = -\mathbf{K}_{uu}^{-1} \mathbf{K}_{u\bar{u}} \Delta\lambda \bar{\mathbf{u}} = \Delta\lambda \hat{\mathbf{u}}, \quad (5)$$

which is nothing but Newton's method. An iteration scheme based on (5) can be simply built by updating the stiffness matrix at each step, i.e., pure Newton's method, or using the same stiffness matrix for multiple iterations (i.e., modified Newton's method). It is well known that Newton's method fails when \mathbf{K}_{uu} is singular or nearly singular, e.g., in or close to limit points of the equilibrium path. In order to overcome this limitation, Riks [1972] proposed to reconstruct the equilibrium path by parametrizing it by its arc length instead of by the parameter λ . This produces a scheme which does not suffer from the convergence problems of Newton's method, while requiring an additional constraint equation. In this scheme we aim to find an equilibrium point $(\mathbf{u}_i + \Delta\mathbf{u} + \dot{\mathbf{u}}, \lambda_i + \Delta\lambda + \dot{\lambda})$ by using as said additional constraint equation a kind of *orthogonality*³ condition between the extrapolation $(\Delta\mathbf{u}, \Delta\lambda)$, given by the Newton's method (see (5)), and Riks's correction $(\dot{\mathbf{u}}, \dot{\lambda})$. Starting from a known equilibrium point $(\mathbf{u}_i, \lambda_i)$, the correction $(\dot{\mathbf{u}}, \dot{\lambda})$ to the Newton extrapolation $(\mathbf{u}_i + \Delta\mathbf{u}, \lambda_i + \Delta\lambda)$ can be computed by exploiting the linearization

$$s[\mathbf{u}_i + \Delta\mathbf{u}, (\lambda_i + \Delta\lambda) \bar{\mathbf{u}}] + \mathbf{K}_{uu} \dot{\mathbf{u}} + \mathbf{K}_{u\bar{u}} \dot{\lambda} \bar{\mathbf{u}} \approx \mathbf{0}, \quad (6)$$

where \mathbf{K}_{uu} and $\mathbf{K}_{u\bar{u}}$ have been defined in the foregoing, but are now computed in $(\mathbf{u}_i + \Delta\mathbf{u}, \lambda_i + \Delta\lambda)$. From (6) we can evaluate $\dot{\mathbf{u}}$ as

$$\dot{\mathbf{u}} = -\mathbf{K}_{uu}^{-1} (s[\mathbf{u}_i + \Delta\mathbf{u}, (\lambda_i + \Delta\lambda) \bar{\mathbf{u}}] + \mathbf{K}_{u\bar{u}} \dot{\lambda} \bar{\mathbf{u}}), \quad (7)$$

³This orthogonality condition will be defined precisely below.

once $\dot{\lambda}$ is known. Clearly, a further equation is needed in order to compensate for the new unknown $\dot{\lambda}$. We use to this aim the condition

$$\begin{bmatrix} \Delta \mathbf{u} \\ \Delta \lambda \bar{\mathbf{u}} \end{bmatrix} \cdot \mathbf{K} \begin{bmatrix} \dot{\mathbf{u}} \\ \dot{\lambda} \bar{\mathbf{u}} \end{bmatrix} = 0, \quad (8)$$

which expresses the *orthogonality* between $(\Delta \mathbf{u}, \Delta \lambda \bar{\mathbf{u}})$ and $(\dot{\mathbf{u}}, \dot{\lambda} \bar{\mathbf{u}})$ in the scalar product defined by the stiffness matrix \mathbf{K} evaluated in $(\mathbf{u}_i + \Delta \mathbf{u}, \lambda_i + \Delta \lambda)$. Indeed, a simple computation gives

$$\dot{\lambda} = - \frac{\Delta \mathbf{u} \cdot \mathbf{K}_{uu} \dot{\mathbf{u}} + \Delta \lambda \bar{\mathbf{u}} \cdot \mathbf{K}_{\bar{u}\bar{u}} \dot{\mathbf{u}}}{\Delta \mathbf{u} \cdot \mathbf{K}_{u\bar{u}} \bar{\mathbf{u}} + \Delta \lambda \bar{\mathbf{u}} \cdot \mathbf{K}_{\bar{u}\bar{u}} \bar{\mathbf{u}}}, \quad (9)$$

and by using (7), (9), and the definitions of $\hat{\mathbf{u}}$ and $\Delta \mathbf{u}$ in (5), we obtain

$$\dot{\lambda} = \frac{\hat{\mathbf{u}} \cdot \mathbf{s} + \bar{\mathbf{u}} \cdot \mathbf{K}_{\bar{u}\bar{u}} \mathbf{K}_{uu}^{-1} \mathbf{s}}{\bar{\mathbf{u}} \cdot (\mathbf{K}_{\bar{u}\bar{u}} - \mathbf{K}_{\bar{u}\bar{u}} \mathbf{K}_{uu}^{-1} \mathbf{K}_{u\bar{u}}) \bar{\mathbf{u}}}, \quad (10)$$

which is the correction for the extrapolation $\Delta \lambda$. Successively, by using (7), we can compute the correction $\dot{\mathbf{u}}$ for the Newton extrapolation $\Delta \mathbf{u}$. We remark that three terms can be distinguished in (10):

- (1) The first addend of the numerator is the work done by the structural reaction $\mathbf{s}[\mathbf{u}_i + \Delta \mathbf{u}, (\lambda_i + \Delta \lambda) \bar{\mathbf{u}}]$ on displacements $\hat{\mathbf{u}}$ of the free nodes.
- (2) The second addend of the numerator complements the above-mentioned work done by the structural reaction on free nodes with the work done by

$$\mathbf{K}_{\bar{u}\bar{u}} \mathbf{K}_{uu}^{-1} \mathbf{s}[\mathbf{u}_i + \Delta \mathbf{u}, (\lambda_i + \Delta \lambda) \bar{\mathbf{u}}]$$

on the constrained displacements $\bar{\mathbf{u}}$. In formulae we have that

$$\mathbf{K}_{\bar{u}\bar{u}} \mathbf{K}_{uu}^{-1} \mathbf{s} = \bar{\mathbf{s}}[\mathbf{u}_i + \Delta \mathbf{u} + \mathbf{K}_{uu}^{-1} \mathbf{s}, (\lambda_i + \Delta \lambda) \bar{\mathbf{u}}] - \bar{\mathbf{s}}[\mathbf{u}_i + \Delta \mathbf{u}, (\lambda_i + \Delta \lambda) \bar{\mathbf{u}}], \quad (11)$$

where $\bar{\mathbf{s}}[\cdot]$ collects entries of the structural reaction corresponding to constrained displacements.

- (3) The denominator can be interpreted as the work done by the structural reaction on the constrained displacements. In formulae we have that

$$\begin{aligned} & (\mathbf{K}_{\bar{u}\bar{u}} - \mathbf{K}_{\bar{u}\bar{u}} \mathbf{K}_{uu}^{-1} \mathbf{K}_{u\bar{u}}) \bar{\mathbf{u}} \\ & \approx \frac{\bar{\mathbf{s}}[\mathbf{u}_i + \Delta \mathbf{u}, (\lambda_i + \Delta \lambda + \delta \lambda) \bar{\mathbf{u}}] - \bar{\mathbf{s}}[\mathbf{u}_i + \Delta \mathbf{u} + \delta \mathbf{u}, (\lambda_i + \Delta \lambda) \bar{\mathbf{u}}]}{\delta \lambda}, \quad (12) \end{aligned}$$

where $\delta \lambda = \alpha \Delta \lambda$, with $\alpha > 0$ (good results are usually obtained using $\alpha = 1$), and

$$\delta \mathbf{u} = \frac{1}{\delta \lambda} \mathbf{K}_{uu}^{-1} (\mathbf{s}[\mathbf{u}_i + \Delta \mathbf{u}, (\lambda_i + \Delta \lambda + \delta \lambda) \bar{\mathbf{u}}] - \mathbf{s}[\mathbf{u}_i + \Delta \mathbf{u}, (\lambda_i + \Delta \lambda) \bar{\mathbf{u}}]). \quad (13)$$

4. Numerical simulations

Solving the Hencky model sketched in Section 2 by exploiting the algorithm briefly depicted in Section 3, we can compute equilibrium paths for pantographic beams. Numerical values employed for simulations are reported in Table 1. For all cases which are here studied, the length of the pantographic beam L is the same. We analyzed pantographic beams with 21 (cases 1 and 3) and 41 (cases 2 and 4) unit cells. Cases 1 and 2 differ from cases 3 and 4 by the presence of additional rotational springs with stiffness d (see Figure 1) on the left and right sides of the pantographic beam. In passing from case 1 to case 2 and from case 3 to case 4, the number of unit cells n_{uc} is almost (due to symmetry reasons) doubled. In addition, in passing from case 1 to case 2 and from case 3 to case 4, we rescaled stiffnesses according to the following law used in [Barchiesi et al. 2018; 2019] for getting the homogenized continuum model as $n_{\text{uc}} \rightarrow \infty$ for fixed total length L :

$$a \sim n_{\text{uc}}^3, \quad b \sim n_{\text{uc}}, \quad c \sim n_{\text{uc}}^{-1}, \quad d \sim n_{\text{uc}}. \quad (14)$$

We notice that $\ell_0 = \|P_j - P_i\|$ in (2) is equal to $\sqrt{2}/(2n_{\text{uc}})$ (here, P_i and P_j are two pivots which share the same extensional spring). Therefore, the product $a\ell_0$, which will be used in the sequel to scale some quantities, depends upon n_{uc} . We also remark that the scaling law (14) entails that $a/b \sim n_{\text{uc}}^2$ and $b/c \sim n_{\text{uc}}^2$. This means that for large values of n_{uc} , complete cell closure in straight (i.e., pantographic mechanism) or acuminate geometry — depending upon cell position and boundary conditions — becomes especially favorable energetically for sufficiently large prescribed displacements

Case study 1. By using the number of unit cells and the values for the stiffnesses reported in the first line of Table 1, we computed the equilibrium path shown in Figure 2 (continuous black line), which is the locus of pairs made up of the value of the constrained displacement at midpoint, represented by the parameter λ , and the corresponding (global) reaction force R at equilibrium.

case	n_{uc}	a	b	c	d
1	21	10000	10.000	0.025000	0
2	41	74421	19.524	0.012805	0
3	21	10000	10.000	0.025000	10.000
4	41	74421	19.524	0.012805	19.524

Table 1. Data, in SI units, used for simulations of a pantographic beam $L = 1.05$ long.

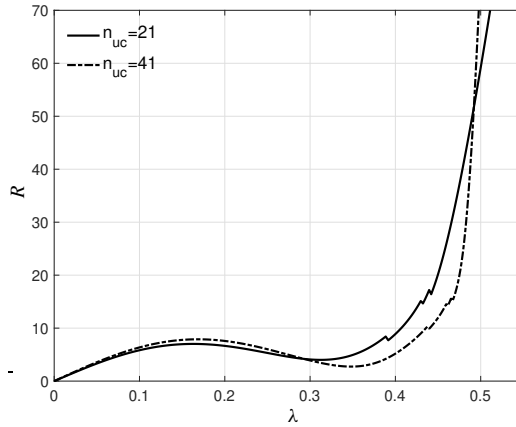


Figure 2. Equilibrium path, i.e., locus of pairs made up of the value of the constrained displacement, λ , at midpoint and the corresponding reaction force R at equilibrium, of the pantographic beam for case 1 (continuous black line) and case 2 (dot-dashed black line).

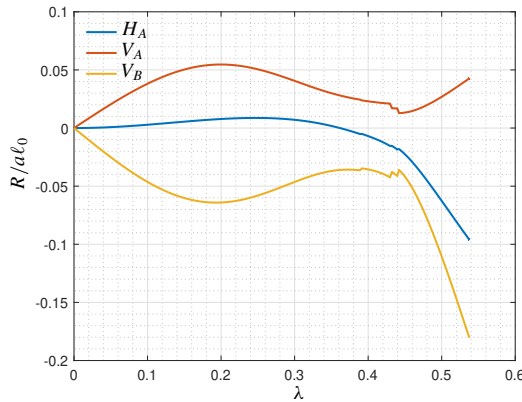


Figure 3. Scaled reactions corresponding to constraints enforced at nodes A and B (H and V are the horizontal and vertical components, respectively) versus λ (case 1).

In addition, we also plot in Figure 3 the reactions — scaled by the product $a\ell_0$ — corresponding to the constraints enforced at nodes A and B — placed on the left of the pantographic beam — versus the constrained vertical displacement λ of the midnode of the structure.

We further plot in Figure 4 the total strain energy — scaled by the product $a\ell_0^2$ — versus the constrained vertical displacement λ at the midnode of the structure. In the same figure we also plot the contributions to the total strain energy — scaled

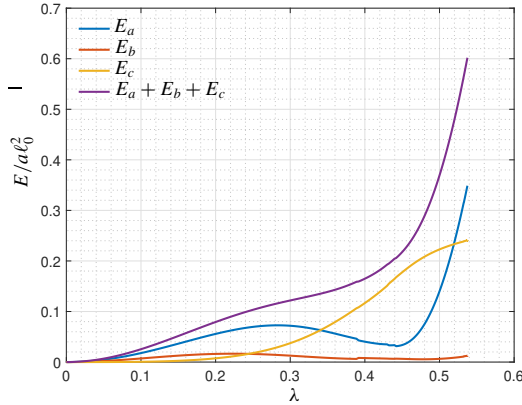


Figure 4. Scaled strain energies versus λ . Stretching E_a , bending E_b , and shearing E_c contribute to total strain energy $E_a + E_b + E_c$ (case 1).

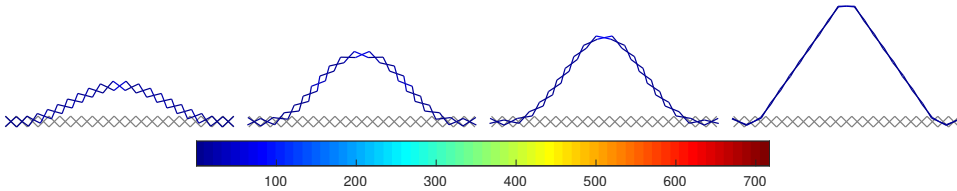


Figure 5. From left to right: deformation corresponding to the local maximum, the local minimum, the stage immediately after the first snap-through, and the last computed point of the equilibrium path reported in Figure 2 with a continuous black line (case 1). Colors indicate the strain energy.

again by the product $\alpha \ell_0^2$ — as distinguished in stretching, bending, and shearing contributions.

Finally, we plot in Figure 5 the current configuration of the system for four values of the parameter λ corresponding to (see Figure 2 (continuous black line)), the local maximum, i.e., limit point, the local minimum, the stage immediately after the first reaction force jump, and the last computed equilibrium point belonging to the increasing branch following the last reaction force jump.

Case study 2. Results for the case study 2 take into account a pantographic beam with 41 unit cells (previously, in case study 1, we used 21 unit cells). The parameters which were used are reported in the second line of Table 1 (stiffnesses in case 1 are rescaled according to (14)). The equilibrium path is plotted in Figure 2 (dot-dashed black line). The two curves in Figure 2 are very close and suggest that independence of the unit cell size $1/n_{uc}$ holds, thus indicating that the scaling

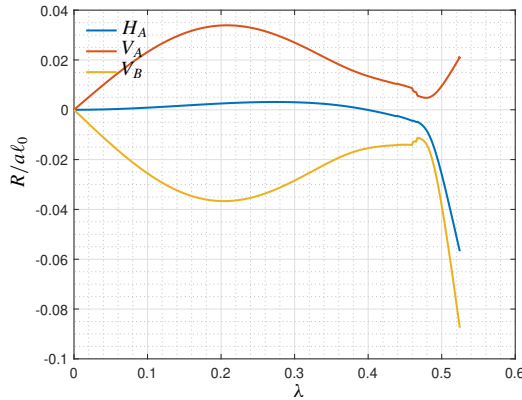


Figure 6. Scaled reactions corresponding to constraints enforced at nodes A and B (H and V are the horizontal and vertical components, respectively), versus λ (case 2).

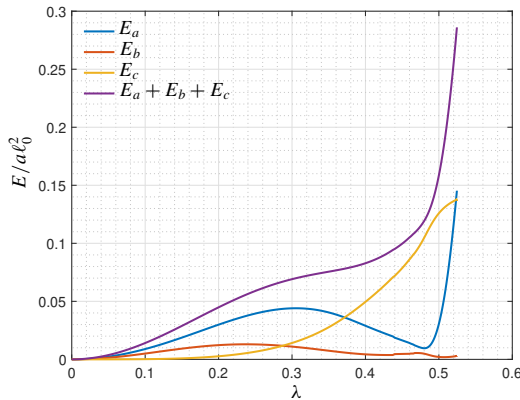


Figure 7. Scaled strain energies versus λ . Stretching E_a , bending E_b , and shearing E_c contribute to total strain energy $E_a + E_b + E_c$ (case 2).

law employed for deriving the homogenized model implies the existence of a limit behavior. The reactions — scaled by the product $a\ell_0$ — corresponding to the constraints enforced at nodes A and B versus the constrained vertical displacement λ of the midnode of the structure are plotted in Figure 6.

The total strain energy — scaled by the product $a\ell_0^2$ — versus the constrained vertical displacement λ at the midnode of the structure is plotted in Figure 7. Contributions to the total strain energy — scaled again by the product $a\ell_0^2$ — as distinguished in stretching, bending, and shearing contributions are also plotted in the same figure.

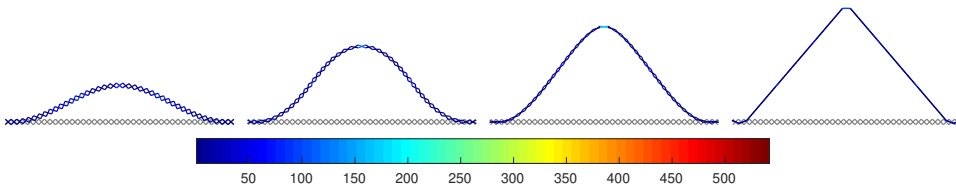


Figure 8. From left to right: deformation corresponding to the local maximum, the local minimum, the stage immediately after the first snap-through, and the last computed point of the equilibrium path reported in Figure 2 with a dot-dashed black line (case 2). Colors indicate the strain energy.

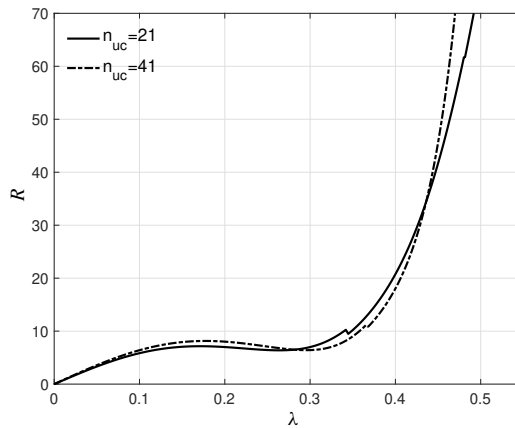


Figure 9. Equilibrium path, i.e., locus of pairs made up of the value of the constrained displacement at midpoint, λ , and the corresponding reaction force R at equilibrium, of the pantographic beam for case 3 (continuous black line) and case 4 (dot-dashed black line).

Figure 8 shows the current configuration of the system for four values of the parameter λ corresponding to (see Figure 2 (dot-dashed black line)) the local maximum, i.e., limit point, the local minimum, the stage immediately after the first reaction force jump, and the last computed equilibrium point belonging to the increasing branch following the last reaction force jump.

Case study 3. Results for the case study 3 take into account a pantographic beam with 21 unit cells. The parameters which were used are reported in the third line of Table 1. The equilibrium path is plotted in Figure 9 (continuous black line).

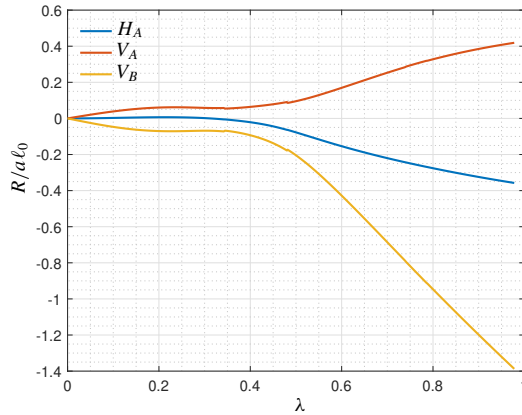


Figure 10. Scaled reactions corresponding to constraints enforced at nodes A and B (H and V are the horizontal and vertical components, respectively) versus λ (case 3).

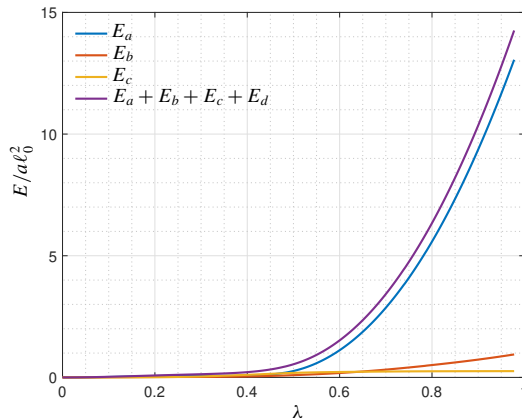


Figure 11. Scaled strain energies versus λ . Stretching E_a , bending E_b , and shearing E_c contribute to total strain energy $E_a + E_b + E_c + E_d$ for stiffness parameters (case 3).

The reactions — scaled by the product $a\ell_0$ — corresponding to the constraints enforced at nodes A and B versus the constrained vertical displacement λ of the midnode of the structure are plotted in Figure 10.

The total strain energy — scaled by the product $a\ell_0^2$ — versus the constrained vertical displacement λ at the midnode of the structure is plotted in Figure 11. Contributions to the total strain energy — scaled again by the product $a\ell_0^2$ — as distinguished in stretching, bending, and shearing contributions are also plotted in the same figure.

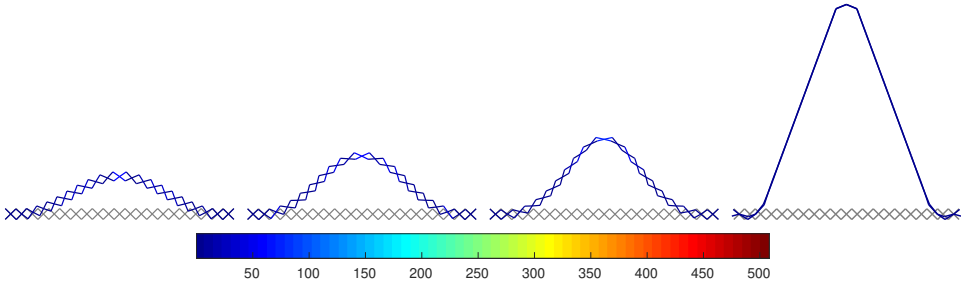


Figure 12. From left to right: deformation corresponding to the local maximum, the local minimum, the stage immediately after the first snap-through, and the last computed point of the equilibrium path reported in Figure 9 with a continuous black line (case 3). Colors indicate the strain energy.

Figure 12 shows the current configuration of the system for four values of the parameter λ corresponding to (see Figure 9 (continuous black line)) the local maximum, i.e., limit point, the local minimum, the stage immediately after the first reaction force jump, and the last computed equilibrium point belonging to the increasing branch following the last reaction force jump.

Case study 4. Results for the case study 4 take into account a pantographic beam with 41 unit cells (previously, in case study 3, we used 21 unit cells). The parameters which were used are reported in the fourth line of Table 1 (stiffnesses in case 3 are rescaled according to (14)). The equilibrium path is plotted in Figure 9 (dashed black line). Again, the curves in Figure 9 are very close and suggest that independence of the unit cell size $1/n_{uc}$ holds, thus indicating that the scaling law employed for deriving the homogenized model implies the existence of a limit behavior. The reactions — scaled by the product al_0 — corresponding to the constraints enforced at nodes A and B versus the constrained vertical displacement λ of the midnode of the structure are plotted in Figure 13.

The total strain energy — scaled by the product al_0^2 — versus the constrained vertical displacement λ at the midnode of the structure is plotted in Figure 14. Contributions to the total strain energy — scaled again by the product al_0^2 — as distinguished in stretching, bending, and shearing contributions are also plotted in the same figure.

Figure 15 shows the current configuration of the system for four values of the parameter λ corresponding to (see Figure 9 (dashed black line)) the local maximum, i.e., limit point, the local minimum, the stage immediately after the first reaction force jump, and the last computed equilibrium point belonging to the increasing branch following the last reaction force jump.

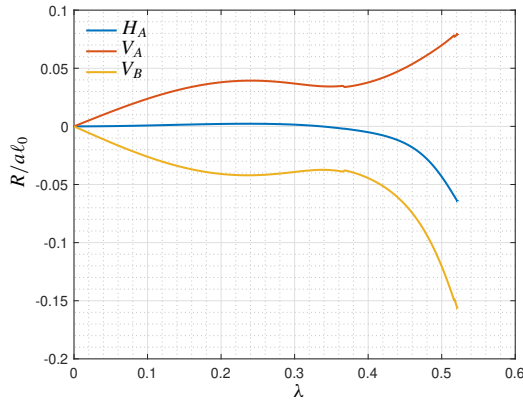


Figure 13. Scaled reactions corresponding to constraints enforced at nodes A and B (H and V are the horizontal and vertical components, respectively) versus λ (case 4).

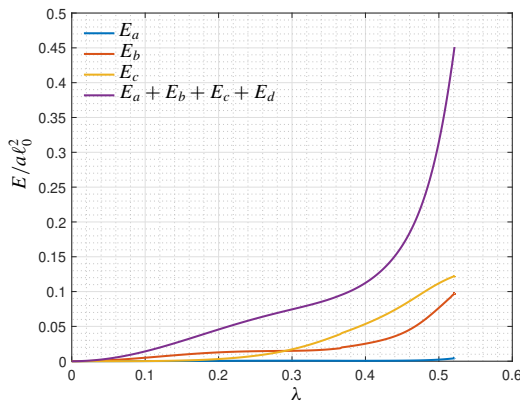


Figure 14. Scaled strain energies versus λ . Stretching E_a , bending E_b , and shearing E_c contribute to total strain energy $E_a + E_b + E_c + E_d$ (case 4).

Sensitivity analysis respect to the stiffness parameters. In addition, we perform an analysis of the equilibrium path sensitivity with respect to changes in stiffness parameters of the pantographic beam subjected to the three-point bending test, which is reported in Figure 16. We observe that, basically, each of the found behaviors can be regarded as a degeneracy of the equilibrium path in Figure 2. The variety of obtained behaviors suggests that tuning of the pantographic beam mechanical response deserves future investigation.

Remarks on numerical simulations. We notice that:

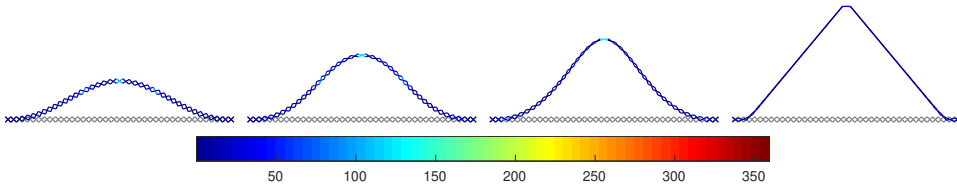


Figure 15. From left to right: deformation corresponding to the local maximum, the local minimum, the stage immediately after the first snap-through, and the last computed point of the equilibrium path reported in Figure 9 with a dot-dashed black line (case 4). Colors indicate the strain energy.

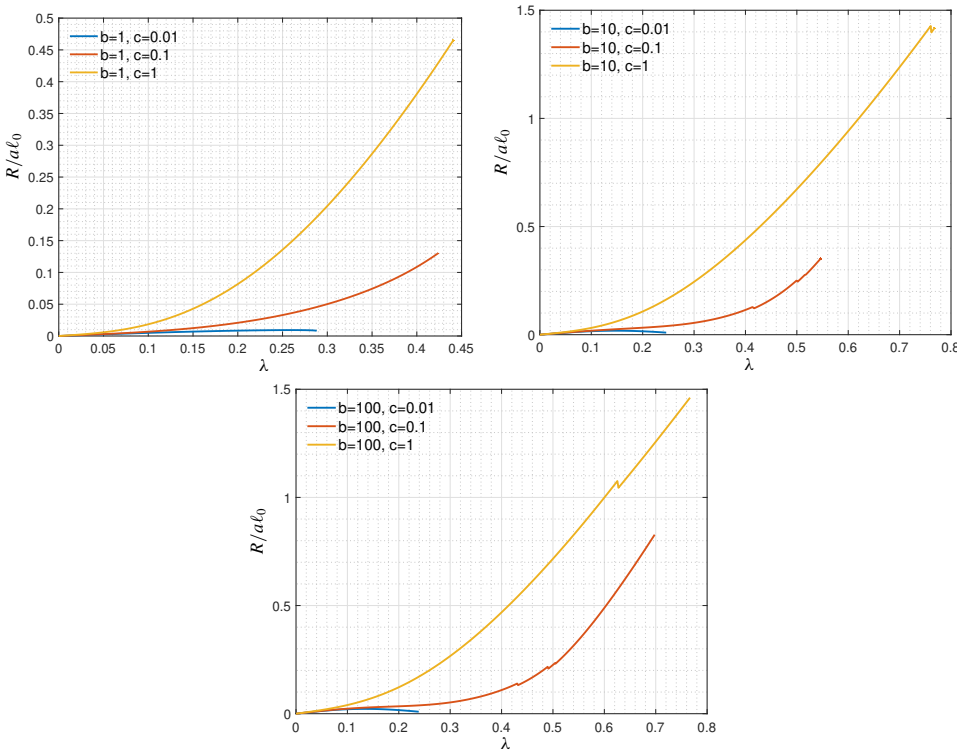


Figure 16. Sensitivity analysis of the equilibrium path respect to the stiffness parameters a , b , and c for the case study 1.

- (1) In all cases, the force-displacement equilibrium paths, in continuous and dashed black line in Figures 2 and 9, show the existence of two limit points, i.e., the tangent to the equilibrium path is horizontal/vertical (horizontal in this case). When increasing the constrained displacement at midpoint, the presence of an increasing reaction branch in the equilibrium path followed by a

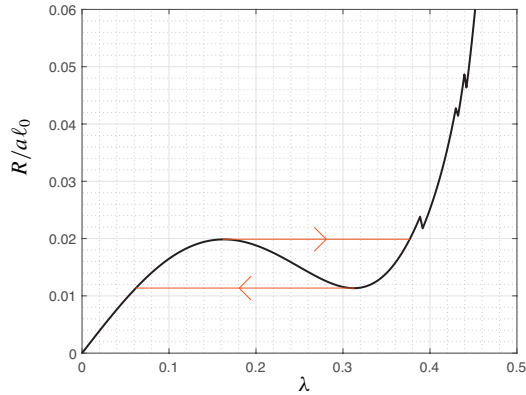


Figure 17. Equilibrium path for case study 1 with indication, in red, of the force-controlled loading-unloading pseudoelastic cycle.

decreasing one, passing through a limit point, gives a well known response (an analogous discussion can be given for the presence of a decreasing reaction branch followed by an increasing one, passing through a limit point). Indeed, it implies that, when considering a monotonically increasing prescribed force acting on the midpoint (therefore, we do not apply any more displacement but force), when the limit point is reached, then the equilibrium displacement experiences a sudden increase (see the red lines in Figure 17 indicating a force-controlled loading-unloading pseudoelastic cycle) [Eremeyev and Lebedev 2006]. We remark that such a phenomenon, which is observed in structures like the von Mises arch, contrarily to said structures, does not involve any local nor global snap-through instability, but it is a geometrical effect. Such an effect can be exploited in multiple applications requiring so-called mechanical switches.

- (2) In all cases three local snap-through instabilities are occurring in the three-point bending problem when varying the constrained vertical displacement, which are signaled in all plots (except for the deformed equilibrium configurations where they can be seen visually) by small bumps. The first snap-through involves the two cells adjacent to the midpoint, while the following two snap-through instabilities occur for two different values of λ at the boundary cells. These two last snap-through instabilities occur for higher values of λ if d increases, as d is in that respect a penalization term.
- (3) The horizontal reaction force H in Figure 3 changes its sign with λ in all cases.
- (4) Looking at Figures 5, 8, 12, and 15, and particularly at points on the centerline of the structure (macroscopic deformed line), with increasing midnode

constrained vertical displacement, for all cases, the structure switches progressively from a macroscopic flexural behavior to an extensional one. This is due to cells exploiting the pantographic mode to minimize the deformation energy of the structure. Such a behavior is further triggered at microscale by the occurrence of local snap-through instabilities. Indeed, cell closure in acuminate shape leads to progressively more and more localized macroscopic flexural deformations (which are unavoidable to fulfill kinematic constraints; in addition, as already mentioned, macroscopic flexure is not energetically penalized in such situation) in the vicinity of constrained nodes where snap-through instabilities are occurring. In all cases, for the highest λ of the computation, macroscopic flexural deformation is completely concentrated in cells adjacent to constrained nodes (see again Figures 5, 8, 12, and 15). Other regions of the beam are macroscopically straight and therefore experience only macroscopic extension. Straight closed cells in the current configuration store energy only in extensional springs. Clearly, the size of this localization depends upon the unit cell size and will degenerate at a point when $n_{uc} \rightarrow \infty$, i.e., at macroscale in the homogenized continuum. It seems then reasonable to conjecture that, at macroscale, the beam will undergo at boundaries and at midpoint a beam-to-cable phase transition and assume for sufficiently large values of λ a triangle shape. All these considerations are reflected in the equilibrium path, which shows with increasing midnode constrained vertical displacement — following the limit point — a decreasing reaction branch (due to not-yet-complete cell closure by pantographic mode) and (following complete cell closure) a successive stiffening controlled by extensional springs (which are according to rescaling law (14) the stiffest ones indeed). The scaled strain energies in Figures 4, 7, 11, and 14 clearly show that deformation energy stored within extensional springs increases superlinearly, reaching values comparable to those of energy stored within flexural-rotational springs at the end of the computation.

5. Concluding remarks and future challenges

It should at this point be clear why the results here reported are to be intended as an aid toward the formulation of conjectures attaining the continuum model and its related degeneracies. Especially, we were motivated in this investigation by understanding which features of the nonlinear behavior of slender pantographic discrete structure are — up to homogenization error (which clearly decreases with n_{uc}) — independent of the unit cell size $1/n_{uc}$ and should be observed in the homogenized continuum model. In this regard, it is worth noting that, in Figures 2 and 9, low sensitivity of the equilibrium path has been observed by increasing the cell number.

Looking at the same figures (and at the other ones) one would conclude that bumps, which correspond to snap-throughs, disappear in the limit of the cell number going to infinity. Nevertheless, it remains an open question whether the observed bumps — i.e., reaction force/energy drop with respect to displacement increase — will tend to have a (smaller) finite amplitude or not. More investigations in this regard are therefore required.

As we mentioned in the introduction, homogenized pantographic beams are complete second-gradient 1D-continua. Such continua have been previously validated by numerical discrete simulations based on Newton's method [Barchiesi et al. 2019]. Clearly, results reported herein should be regarded also as an extension of such previous work. Indeed, while solving the macromodel for prescribed (large) displacements up to an apparent negative stiffness regime — passing through the occurrence of limit points — was possible, that was up to now not possible for the micromodel.

In this respect, owing to the results obtained herein, we are able to state that simulations at microlevel confirm the predictions of the homogenized continuum. It is therefore possible to conclude that such negative stiffness effects and the occurrence of limit points in the equilibrium path, which are due to collective concurrence of geometric and mechanical properties of single elements (and not due to any local or global snap-through) arranged in pantographic topology, is mainly controlled at macroscale by second-gradient effects, i.e., at microscale by pantographic mechanism, as opposed to bending effects.

Finally, we list some challenges that surely will be tackled in the near future:

- (1) The extension to 3D cases in order to take into account out-of-plane displacements; see [Giorgio et al. 2017b] for a continuum model able to predict out-of-plane bifurcations and [Turco 2018a; Eugster et al. 2014] for a first attempt to model 3D inextensible beams using the Hencky guidelines.
- (2) Some technical applications require removing the hypothesis of quasistatic application of external loads or given displacements; in these cases we have to consider inertia forces following the suggestions reported in [Giorgio et al. 2017a; Engelbrecht and Berezovski 2015; Tahaei Yaghoubi et al. 2018].
- (3) Stiffness parameters of the pantographic beam have been chosen starting from estimates derived from global parameters of the continuum model; however, any methods capable of correlating experimental results with the stiffness parameters of the proposed model are surely interesting; see, e.g., [Placidi et al. 2015].
- (4) Here we used simple laws to describe extensional, flexural, and shearing interaction; however, other interaction laws might be considered, e.g., those

reported in [Braides and Solci 2016; Atai and Steigmann 1997; Challamel et al. 2014].

- (5) Since the pantographic beam presented in the foregoing could be regarded as the representative volume element for continuum models and since, to obtain quantitative results in general problems, continuum models have to be discretized, it appears interesting to consider modern interpolations laws based on B-splines and NURBS; see, for an insight, [Greco et al. 2017; Greco and Cuomo 2013; Cuomo et al. 2014; Balobanov and Niiranen 2018].
- (6) Hencky models are the fundamental building block for continuum models such as, e.g., those presented in [Khakalo et al. 2018; Seppecher 1996; Pideri and Seppecher 1997a; 1997b; Scala and Van Goethem 2016; Lurie and Kalamkarov 2007; Gusev and Lurie 2017; Giorgio 2016; Abali et al. 2016; Misra and Poorsolhjouy 2015; 2017; Shirani et al. 2019; De Masi et al. 2008; 2009; Carlen et al. 2009; Braides et al. 2009]; therefore, the developments of new and efficient Hencky models, besides to be useful to build reference results as shown in this paper, are surely a valuable contribution towards the construction of continuum models; see also [dell’Isola et al. 2017] for a historical framework and [Reiher et al. 2017] for some insight about the computational point of view.
- (7) Even though the results presented here consider only elastic deformation patterns, it is possible to build Lagrangian models including damaging [Turco et al. 2016d]; furthermore, it is possible to include novel direct continuum modeling proposed in [Placidi and Barchiesi 2018; Giorgio and Scerrato 2017; Placidi et al. 2018; Shirani et al. 2017; Ganghoffer and Pastrone 2009].

References

- [Abali et al. 2016] B. E. Abali, C.-C. Wu, and W. H. Müller, “An energy-based method to determine material constants in nonlinear rheology with applications”, *Continuum Mech. Therm.* **28**:5 (2016), 1221–1246.
- [Alibert et al. 2003] J.-J. Alibert, P. Seppecher, and F. Dell’Isola, “Truss modular beams with deformation energy depending on higher displacement gradients”, *Math. Mech. Solids* **8**:1 (2003), 51–73.
- [Atai and Steigmann 1997] A. A. Atai and D. J. Steigmann, “On the nonlinear mechanics of discrete networks”, *Arch. Appl. Mech.* **67**:5 (1997), 303–319.
- [Balobanov and Niiranen 2018] V. Balobanov and J. Niiranen, “Locking-free variational formulations and isogeometric analysis for the Timoshenko beam models of strain gradient and classical elasticity”, *Comput. Methods Appl. Mech. Eng.* **339** (2018), 137–159.
- [Barchiesi et al. 2018] E. Barchiesi, F. dell’Isola, M. Laudato, L. Placidi, and P. Seppecher, “A 1D continuum model for beams with pantographic microstructure: asymptotic micro-macro identification and numerical results”, pp. 43–74 in *Advances in mechanics of microstructured media and structures*, edited by F. dell’Isola et al., Adv. Struct. Mater. **87**, Springer, 2018.

- [Barchiesi et al. 2019] E. Barchiesi, S. R. Eugster, L. Placidi, and F. dell’Isola, “Pantographic beam: a complete second gradient 1D-continuum in plane”, *Z. Angew. Math. Phys.* **70**:5 (2019), art. id. 135.
- [Bertoldi et al. 2017] K. Bertoldi, V. Vitelli, J. Christensen, and M. van Hecke, “Flexible mechanical metamaterials”, *Nat. Rev. Mater.* **2** (2017), art. id. 17066.
- [Braides and Solci 2016] A. Braides and M. Solci, “Asymptotic analysis of Lennard-Jones systems beyond the nearest-neighbour setting: a one-dimensional prototypical case”, *Math. Mech. Solids* **21**:8 (2016), 915–930.
- [Braides et al. 2009] A. Braides, G. Riey, and M. Solci, “Homogenization of Penrose tilings”, *C. R. Math. Acad. Sci. Paris* **347**:11–12 (2009), 697–700.
- [Carlen et al. 2009] E. A. Carlen, M. C. Carvalho, R. Esposito, J. L. Lebowitz, and R. Marra, “Droplet minimizers for the Gates–Lebowitz–Penrose free energy functional”, *Nonlinearity* **22**:12 (2009), 2919–2952.
- [Challamel et al. 2014] N. Challamel, J. Lerbet, and C. M. Wang, “On buckling of granular columns with shear interaction: discrete versus nonlocal approaches”, *J. Appl. Phys.* **115**:23 (2014), art. id. 234902.
- [Cuomo et al. 2014] M. Cuomo, L. Contrafatto, and L. Greco, “A variational model based on isogeometric interpolation for the analysis of cracked bodies”, *Int. J. Eng. Sci.* **80** (2014), 173–188.
- [De Masi et al. 2008] A. De Masi, I. Merola, E. Presutti, and Y. Vignaud, “Potts models in the continuum: uniqueness and exponential decay in the restricted ensembles”, *J. Stat. Phys.* **133**:2 (2008), 281–345.
- [De Masi et al. 2009] A. De Masi, I. Merola, E. Presutti, and Y. Vignaud, “Coexistence of ordered and disordered phases in Potts models in the continuum”, *J. Stat. Phys.* **134**:2 (2009), 243–306.
- [dell’Isola et al. 2016] F. dell’Isola, I. Giorgio, M. Pawlikowski, and N. L. Rizzi, “Large deformations of planar extensible beams and pantographic lattices: heuristic homogenization, experimental and numerical examples of equilibrium”, *P. Roy. Soc. A Math. Phys.* **472**:2185 (2016), art. id. 20150790.
- [dell’Isola et al. 2017] F. dell’Isola, A. Della Corte, and I. Giorgio, “Higher-gradient continua: the legacy of Piola, Mindlin, Sedov and Toupin and some future research perspectives”, *Math. Mech. Solids* **22**:4 (2017), 852–872.
- [dell’Isola et al. 2019a] F. dell’Isola, P. Seppecher, J. J. Alibert, T. Lekszycki, R. Grygoruk, M. Pawlikowski, D. Steigmann, I. Giorgio, U. Andreaus, E. Turco, M. Gołaszewski, N. Rizzi, C. Boutin, V. A. Eremeyev, A. Misra, L. Placidi, E. Barchiesi, L. Greco, M. Cuomo, A. Cazzani, A. Della Corte, A. Battista, D. Scerrato, I. Zurba Eremeeva, Y. Rahali, J.-F. Ganghoffer, W. Müller, G. Ganzosch, M. Spagnuolo, A. Pfaff, K. Barcz, K. Hoschke, J. Neggers, and F. Hild, “Pantographic metamaterials: an example of mathematically driven design and of its technological challenges”, *Continuum Mech. Therm.* **31**:4 (2019), 851–884.
- [dell’Isola et al. 2019b] F. dell’Isola, P. Seppecher, M. Spagnuolo, E. Barchiesi, F. Hild, T. Lekszycki, I. Giorgio, L. Placidi, U. Andreaus, M. Cuomo, S. R. Eugster, A. Pfaff, K. Hoschke, R. Langkemper, E. Turco, R. Sarikaya, A. Misra, M. De Angelo, F. D’Annibale, A. Bouterf, X. Pinelli, A. Misra, B. Desmorat, M. Pawlikowski, C. Dupuy, D. Scerrato, P. Peyre, M. Laudato, L. Manzari, P. Göransson, C. Hesch, S. Hesch, P. Franciosi, J. Dirrenberger, F. Maurin, Z. Vangelatos, C. Grigoropoulos, V. Melissinaki, M. Farsari, W. Müller, B. Emek Abali, C. Liebold, G. Ganzosch, P. Harrison, R. Drobnicki, L. Igumnov, F. Alzahrani, and T. Hayat, “Advances in pantographic structures: design, manufacturing, models, experiments and image analyses”, *Continuum Mech. Therm.* **31**:4 (2019), 1231–1282.

- [dell’Isola et al. 2019c] F. dell’Isola, E. Turco, A. Misra, Z. Vangelatos, C. Grigoropoulos, V. Melissinaki, and M. Farsari, “Force–displacement relationship in micro-metric pantographs: experiments and numerical simulations”, *C. R. Mécanique* **347**:5 (2019), 397–405.
- [Engelbrecht and Berezovski 2015] J. Engelbrecht and A. Berezovski, “Reflections on mathematical models of deformation waves in elastic microstructured solids”, *Math. Mech. Complex Syst.* **3**:1 (2015), 43–82.
- [Eremeyev and Lebedev 2006] V. A. Eremeyev and L. P. Lebedev, “On the loss stability of von Mises truss with the effect of pseudo-elasticity”, *Mat. Enseñ. Univ. (N. S.)* **14**:2 (2006), 111–118.
- [Eugster et al. 2014] S. R. Eugster, C. Hesch, P. Betsch, and C. Glocker, “Director-based beam finite elements relying on the geometrically exact beam theory formulated in skew coordinates”, *Int. J. Numer. Methods Eng.* **97**:2 (2014), 111–129.
- [Filipov et al. 2015] E. T. Filipov, T. Tachi, and G. H. Paulino, “Origami tubes assembled into stiff, yet reconfigurable structures and metamaterials”, *P. Natl. Acad. Sci. USA* **112**:40 (2015), 12321–12326.
- [Ganghoffer and Pastrone 2009] J.-F. Ganghoffer and F. Pastrone (editors), *Mechanics of microstructured solids: cellular materials, fibre reinforced solids and soft tissues*, Lecture Notes in Applied and Computational Mechanics **46**, Springer, 2009.
- [Giorgio 2016] I. Giorgio, “Numerical identification procedure between a micro-Cauchy model and a macro-second gradient model for planar pantographic structures”, *Z. Angew. Math. Phys.* **67**:4 (2016), art. id. 95.
- [Giorgio and Scerrato 2017] I. Giorgio and D. Scerrato, “Multi-scale concrete model with rate-dependent internal friction”, *Eur. J. Environ. Civ. Eng.* **21**:7–8 (2017), 821–839.
- [Giorgio et al. 2017a] I. Giorgio, A. Della Corte, and F. dell’Isola, “Dynamics of 1D nonlinear pantographic continua”, *Nonlinear Dynam.* **88**:1 (2017), 21–31.
- [Giorgio et al. 2017b] I. Giorgio, N. L. Rizzi, and E. Turco, “Continuum modelling of pantographic sheets for out-of-plane bifurcation and vibrational analysis”, *P. Roy. Soc. A Math. Phys.* **473**:2207 (2017), art. id. 20170636.
- [Greco and Cuomo 2013] L. Greco and M. Cuomo, “B-spline interpolation of Kirchhoff–Love space rods”, *Comput. Methods Appl. Mech. Eng.* **256** (2013), 251–269.
- [Greco et al. 2017] L. Greco, M. Cuomo, L. Contrafatto, and S. Gazzo, “An efficient blended mixed B-spline formulation for removing membrane locking in plane curved Kirchhoff rods”, *Comput. Methods Appl. Mech. Eng.* **324** (2017), 476–511.
- [Gusev and Lurie 2017] A. A. Gusev and S. A. Lurie, “Symmetry conditions in strain gradient elasticity”, *Math. Mech. Solids* **22**:4 (2017), 683–691.
- [Khakalo et al. 2018] S. Khakalo, V. Balobanov, and J. Niiranen, “Modelling size-dependent bending, buckling and vibrations of 2D triangular lattices by strain gradient elasticity models: applications to sandwich beams and auxetics”, *Int. J. Eng. Sci.* **127** (2018), 33–52.
- [Lurie and Kalamkarov 2007] S. A. Lurie and A. L. Kalamkarov, “General theory of continuous media with conserved dislocations”, *Int. J. Solids Struct.* **43**:22–23 (2007), 7468–7485.
- [Misra and Poorsolhjouy 2015] A. Misra and P. Poorsolhjouy, “Identification of higher-order elastic constants for grain assemblies based upon granular micromechanics”, *Math. Mech. Complex Syst.* **3**:3 (2015), 285–308.
- [Misra and Poorsolhjouy 2017] A. Misra and P. Poorsolhjouy, “Elastic behavior of 2D grain packing modeled as micromorphic media based on granular micromechanics”, *J. Eng. Mech.* **143**:1 (2017), art. id. C4016005.

- [Pideri and Seppecher 1997a] C. Pideri and P. Seppecher, “A second gradient material resulting from the homogenization of an heterogeneous linear elastic medium”, *Continuum Mech. Therm.* **9**:5 (1997), 241–257.
- [Pideri and Seppecher 1997b] C. Pideri and P. Seppecher, “Un résultat d’homogénéisation pour un matériau élastique renforcé périodiquement par des fibres élastiques de très grande rigidité”, *C. R. Acad. Sci. IIB Mec.* **324**:8 (1997), 475–481.
- [Placidi and Barchiesi 2018] L. Placidi and E. Barchiesi, “Energy approach to brittle fracture in strain-gradient modelling”, *P. Roy. Soc. A Math. Phys.* **474**:2210 (2018), art. id. 20170878.
- [Placidi et al. 2015] L. Placidi, U. Andreaus, A. D. Corte, and T. Lekszycki, “Gedanken experiments for the determination of two-dimensional linear second gradient elasticity coefficients”, *Z. Angew. Math. Phys.* **66**:6 (2015), 3699–3725.
- [Placidi et al. 2018] L. Placidi, E. Barchiesi, and A. Misra, “A strain gradient variational approach to damage: a comparison with damage gradient models and numerical results”, *Math. Mech. Complex Syst.* **6**:2 (2018), 77–100.
- [Reiher et al. 2017] J. C. Reiher, I. Giorgio, and A. Bertram, “Finite-element analysis of polyhedra under point and line forces in second-strain gradient elasticity”, *J. Eng. Mech.* **143**:2 (2017), art. id. 04016112.
- [Riks 1972] E. Riks, “The application of Newton’s method to the problem of elastic stability”, *J. Appl. Mech. T. ASME* **39**:4 (1972), 1060–1065.
- [Scala and Van Goethem 2016] R. Scala and N. Van Goethem, “Constraint reaction and the Peach–Koehler force for dislocation networks”, *Math. Mech. Complex Syst.* **4**:2 (2016), 105–138.
- [Seppecher 1996] P. Seppecher, “Moving contact lines in the Cahn–Hilliard theory”, *Int. J. Eng. Sci.* **34**:9 (1996), 977–992.
- [Shirani et al. 2017] M. Shirani, M. T. Andani, M. Kadkhodaei, and M. Elahinia, “Effect of loading history on phase transition and martensitic detwinning in shape memory alloys: limitations of current approaches and development of a 1D constitutive model”, *J. Alloy. Comp.* **729** (2017), 390–406.
- [Shirani et al. 2019] M. Shirani, C. Luo, and D. J. Steigmann, “Cosserat elasticity of lattice shells with kinematically independent flexure and twist”, *Continuum Mech. Therm.* **31**:4 (2019), 1087–1097.
- [Tahaei Yaghoubi et al. 2018] S. Tahaei Yaghoubi, V. Balabanov, S. M. Mousavi, and J. Niiranen, “Variational formulations and isogeometric analysis for the dynamics of anisotropic gradient-elastic Euler–Bernoulli and shear-deformable beams”, *Eur. J. Mech. A Solids* **69** (2018), 113–123.
- [Turco 2018a] E. Turco, “Discrete is it enough? The revival of Piola–Hencky keynotes to analyze three-dimensional *elastica*”, *Continuum Mech. Therm.* **30**:5 (2018), 1039–1057.
- [Turco 2018b] E. Turco, “In-plane shear loading of granular membranes modeled as a Lagrangian assembly of rotating elastic particles”, *Mech. Res. Commun.* **92** (2018), 61–66.
- [Turco and Rizzi 2016] E. Turco and N. L. Rizzi, “Pantographic structures presenting statistically distributed defects: numerical investigations of the effects on deformation fields”, *Mech. Res. Commun.* **77** (2016), 65–69.
- [Turco et al. 2016a] E. Turco, K. Barcz, M. Pawlikowski, and N. L. Rizzi, “Non-standard coupled extensional and bending bias tests for planar pantographic lattices, I: numerical simulations”, *Z. Angew. Math. Phys.* **67**:5 (2016), art. id. 122.
- [Turco et al. 2016b] E. Turco, K. Barcz, and N. L. Rizzi, “Non-standard coupled extensional and bending bias tests for planar pantographic lattices, II: comparison with experimental evidence”, *Z. Angew. Math. Phys.* **67**:5 (2016), art. id. 123.

- [Turco et al. 2016c] E. Turco, F. dell’Isola, A. Cazzani, and N. L. Rizzi, “Hencky-type discrete model for pantographic structures: numerical comparison with second gradient continuum models”, *Z. Angew. Math. Phys.* **67**:4 (2016), art. id. 85.
- [Turco et al. 2016d] E. Turco, F. dell’Isola, N. L. Rizzi, R. Grygoruk, W. H. Müller, and C. Liebold, “Fiber rupture in sheared planar pantographic sheets: numerical and experimental evidence”, *Mech. Res. Commun.* **76** (2016), 86–90.
- [Turco et al. 2016e] E. Turco, M. Golaszewski, A. Cazzani, and N. L. Rizzi, “Large deformations induced in planar pantographic sheets by loads applied on fibers: experimental validation of a discrete Lagrangian model”, *Mech. Res. Commun.* **76** (2016), 51–56.
- [Turco et al. 2017a] E. Turco, I. Giorgio, A. Misra, and F. dell’Isola, “King post truss as a motif for internal structure of (meta)material with controlled elastic properties”, *Roy. Soc. Open Sci.* **4**:10 (2017), art. id. 171153.
- [Turco et al. 2017b] E. Turco, M. Golaszewski, I. Giorgio, and F. D’Annibale, “Pantographic lattices with non-orthogonal fibres: experiments and their numerical simulations”, *Compos. B Eng.* **118** (2017), 1–14.
- [Turco et al. 2018] E. Turco, A. Misra, M. Pawlikowski, F. dell’Isola, and F. Hilde, “Enhanced Piola–Hencky discrete models for pantographic sheets with pivots without deformation energy: numerics and experiments”, *Int. J. Solids Struct.* **147** (2018), 94–109.
- [Turco et al. 2019a] E. Turco, F. dell’Isola, and A. Misra, “A nonlinear Lagrangian particle model for grains assemblies including grain relative rotations”, *Int. J. Numer. Anal. Met.* **43**:5 (2019), 1051–1079.
- [Turco et al. 2019b] E. Turco, A. Misra, R. Sarikaya, and T. Lekszycki, “Quantitative analysis of deformation mechanisms in pantographic substructures: experiments and modeling”, *Continuum Mech. Therm.* **31**:1 (2019), 209–223.

Received 3 Jul 2019. Accepted 1 Dec 2019.

EMILIO TURCO: emilio.turco@uniss.it

Dipartimento di Architettura, Design e Urbanistica, Università degli Studi di Sassari, Sassari, Italy

EMILIO BARCHIESI: barchiesiemilio@gmail.com

Dipartimento di Ingegneria Strutturale e Geotecnica, Università degli Studi di Roma “La Sapienza”, Roma, Italy

